

Supporting Information for:

Elucidating the role of reactive nitrogen intermediates in hetero-cyclization during hydrothermal liquefaction of food waste

Heather O. LeClerc¹, Rasha Atwi², Sydney F. Niles³, Amy M. McKenna³, Michael T. Timko¹, Richard H. West², Andrew R. Teixeira^{1*}

¹Department of Chemical Engineering, Worcester Polytechnic Institute, 100 Institute Road, Worcester, MA, 01609, USA

²Department of Chemical Engineering, Northeastern University, 360 Huntington Avenue, 201 Cullinane, Boston, MA, 02115, USA

³National High Magnetic Field Laboratory, 1800 Paul Dirac Dr, Tallahassee, FL, 32310, USA

Methods

$\Delta^\ddagger G^\circ$ Calculation

The free energy barrier of the transition state ($\Delta^\ddagger G^\circ$) uses the parameters from the modified Arrhenius expression $k = A \left(\frac{T}{1K}\right)^n \exp\left(-\frac{Ea}{RT}\right)$ and the Eyring equation for transition state theory $k = \kappa \frac{k_b}{h} T \exp\left(-\frac{\Delta^\ddagger G^\circ}{RT}\right) c^{1-m}$ where c is the standard concentration, or 1 bar / RT with standard state of 1 bar. From the Eyring equation, a transmission coefficient κ of one is assumed, and the Gibbs Free Energy of activation is derived: $\Delta^\ddagger G^\circ = -RT \ln\left(k \left(\frac{1 \text{ bar}}{RT}\right)^{m-1} \frac{h}{k_b T}\right)$. Then the rate coefficients were evaluated and $\Delta^\ddagger G^\circ$ was calculated at the desired temperature (600 K).

GC-MS

Biocrude samples were dissolved in acetone at a ratio of 3 mg/mL for analysis with gas chromatography. The GC-MS consisted of a GC-2010 Plus gas chromatograph coupled with a QP2010 SE mass spectrometer and an AOC-20i autoinjector (Shimadzu Co., Kyoto, Japan). The column used was an SHRXI-5MS (30 m \times 0.25 mm ID \times 0.5 μ m film thickness) (Restek Co., Bellefonte, PA), run with an injection temperature of 290 °C and an ion source temperature of 260 °C. 3 μ L of sample was injected into the GC-MS in split mode (25:1) with a constant flow of helium carrier gas (3.0 mL/min).

The temperature program was set to start at 30 °C for 4 minutes followed by heating at 3 °C/min to 290 °C and held for 5 min. The mass spectrometer was operated in ionization energy in m/z 35 – 500 scan range. Chromatogram peaks were then evaluated using the GCsolution station (Shimadzu Co., Kyoto, Japan). Peak identities were compared with the NIST Mass Spectral Database (NIST11) with all peaks having a confidence greater than 85%.

(+) APPI FT-ICR MS at 9.4 tesla

Biocrude and aqueous samples were dissolved to a final concentration of 125 $\mu\text{g/mL}$ in toluene for analysis via (+) APPI FT-ICR MS at a flow rate of 50 $\mu\text{L/min}$. Toluene increases the ionization efficiency for nonpolar aromatic compounds through dopant-assisted APPI^{1, 2} through charge exchange,^{3, 4} and proton transfer⁵ reactions between ionized toluene molecules and neutral analyte molecules as previously reported. An atmospheric pressure photoionization (APPI) source (Thermo-Fisher Scientific, San Jose, CA) was coupled to the first stage of a custom-built FT-ICR mass spectrometer (see below) through a custom-built interface.⁶ The tube lens was set to 50 V (to minimize ion fragmentation) and heated metal capillary current was 4.5 A. A Hamilton gastight syringe (5.0 mL) and syringe pump were used to deliver the sample (50 $\mu\text{L/min}$) to the heated vaporizer region (350 °C) of the APPI source, where N₂ sheath gas (50 psi) facilitates nebulization. After nebulization, gas-phase neutral analyte molecules exit the heated vaporizer region as a confined jet. A krypton vacuum ultraviolet gas discharge lamp (Syagen Technology, Inc., Tustin, CA) produces 10–10.2 eV photons (120 nm).

All samples were analyzed with a custom-built FT-ICR mass spectrometer⁷ equipped with a 22 cm horizontal room temperature bore 9.4 T superconducting solenoid magnet (Oxford Instruments, Abingdon, U.K.), and a modular ICR data station (Predator)⁸ facilitated instrument control, data acquisition, and data analysis. Positive ions generated at atmospheric pressure enter the skimmer region (~2 Torr) through a heated metal capillary, pass through the first radiofrequency (rf)-only octopole, pass through an rf-only quadrupole, and are externally accumulated⁹ (25–50 ms) in a second octopole equipped with tilted wire extraction electrodes for improved ion extraction and transmission.¹⁰ Helium gas introduced during accumulation cools ions upon collision prior to transfer through rf-only quadrupoles (total length 127 cm) (into a 7-segment open cylindrical cell with capacitively coupled excitation electrodes based on the Tolmachev configuration.^{11, 12} 100 individual transients of 6.8 s duration were signal averaged. The data was collected at the maximum memory depth of the data station hardware (16 million samples), apodized with a single sided Hanning apodization, zero-filled to 16 megasample (16777216 samples or 224). An additional zero fill brings the preFT data packet to 32 megasample, which in turn is processed via absorption-mode FT analysis.^{13, 14} Experimentally measured masses were converted from the International Union of Pure and Applied Chemistry (IUPAC) mass scale to the Kendrick mass scale¹⁵ for rapid identification of homologous series for each heteroatom class (i.e., species with the same C_cH_hN_nO_oS_s content, differing only by degree of alkylation)¹⁶

For each elemental composition, C_cH_hN_nO_oS_s, the heteroatom class, type, double bond equivalents, (DBE = number of rings plus double bonds to carbon, $\text{DBE} = \text{C} - \text{h}/2 + \text{n}/2 + 1$),¹⁷ and carbon number, c, were tabulated for subsequent generation of heteroatom class relative abundance distributions and graphical relative-abundance weighted DBE versus carbon number images. Peaks with signal magnitude greater than 6 times the baseline root-mean-square noise at m/z 500 were exported to peak lists, internally calibrated based on the “walking calibration”¹⁸ and molecular formula assignments and data visualization were performed with PetroOrg software¹⁹ Molecular formula assignments with an error >0.5 ppm were discarded, and only chemical classes with a combined relative abundance of $\geq 0.15\%$ of the total were considered. For all mass spectra,

the achieved spectral resolving power approached the theoretical limit over the entire mass range: for example, average resolving power, $m/\Delta m_{50\%}$, in which $\Delta m_{50\%}$ is mass spectral peak full width at half-maximum peak height, was $\sim 1\,000\,000$ – $1\,500\,000$ at m/z 500.

Results

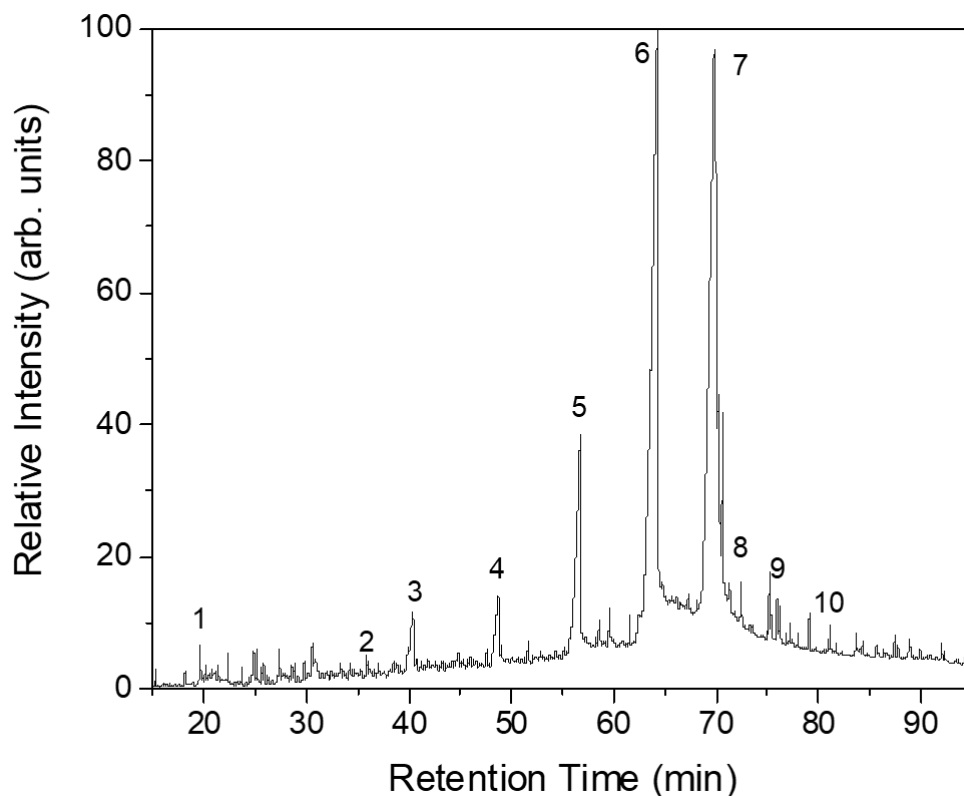
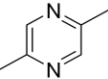
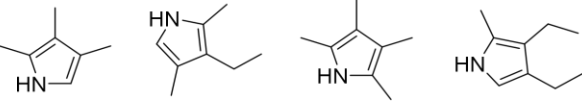
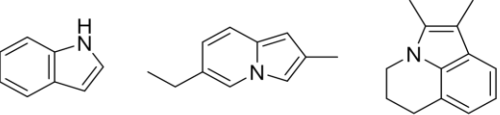
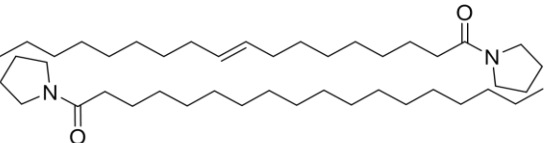
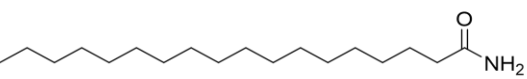


Figure S1. GC-MS chromatogram for food waste HTL oil. Hydrothermal liquefaction was performed at 15 w% organics loading at 300 °C for 1 h. Labeled peaks are as follows: (1) 2,3,4-Trimethylpyrrole, (2) Indole, (3) n-Decanoic acid, (4) Dodecanoic acid, (5) Tetradecanoic acid, (6) Hexadecanoic acid, (7) Octadecanoic acid (8) Octadecanamide, (9) N-Methyldodecanamide, (10) 1-(1-oxooctadecyl) pyrrolidine.

Table S1. Molecular structure of the identified nitrogen heterocycles and one amide structure. Amide chain length range from C₁₂ – C₁₈.

Pyrazine	
Pyrrole	
Indole	
Pyrrolidine	
Amide	

GC×GC-HRT Method

GC×GC-HRT chromatographic analysis was performed on a LECO Pegasus GC×GCHRT 4D system consisting of an Agilent 7890B GC configured with a LECO LPAL3 split/splitless auto-injector system and a dual stage cryogenic modulator (LECO, Saint Joseph, Michigan). Samples were injected in splitless mode. The cold jet gas was dry N₂ chilled with liquid N₂. The hot jet temperature offset was 15 °C above the temperature of the main GC oven and the inlet temperature was isothermal at 310 °C. Two capillary GC columns were utilized in this GC×GC experiment. The first-dimension column was an SGE BPX-50, (60-m length, 0.25 mm I.D., 0.25 μm df) and second-dimension separations were performed on an SGE BPX-50 (2-m length, 0.25 mm I.D., 0.25 μm df). The temperature program of the main oven was held isothermal at 80 °C (12.5 min) and was then ramped from 80 to 330 °C at 1.25 °C min⁻¹. The hot jet pulse width was 2 seconds with a modulation period of 8 seconds. The second-dimension oven was held isothermal at 85 °C (12.5 min) and was then ramped from 85 to 335 °C at 1.25 °C min⁻¹. The carrier gas was helium at a flow rate of 1 mL min⁻¹. Mass resolution was +/- 0.0005 amu. HR-TOF data was sampled at an acquisition rate of 200 spectra per second (actual data collection rate was 187.5 spectra per second) in the mass range of 40 to 700 amu. The ionization method was EI with an Electron Energy of -70 Volts and the Extraction Frequency was 1.5 kHz.

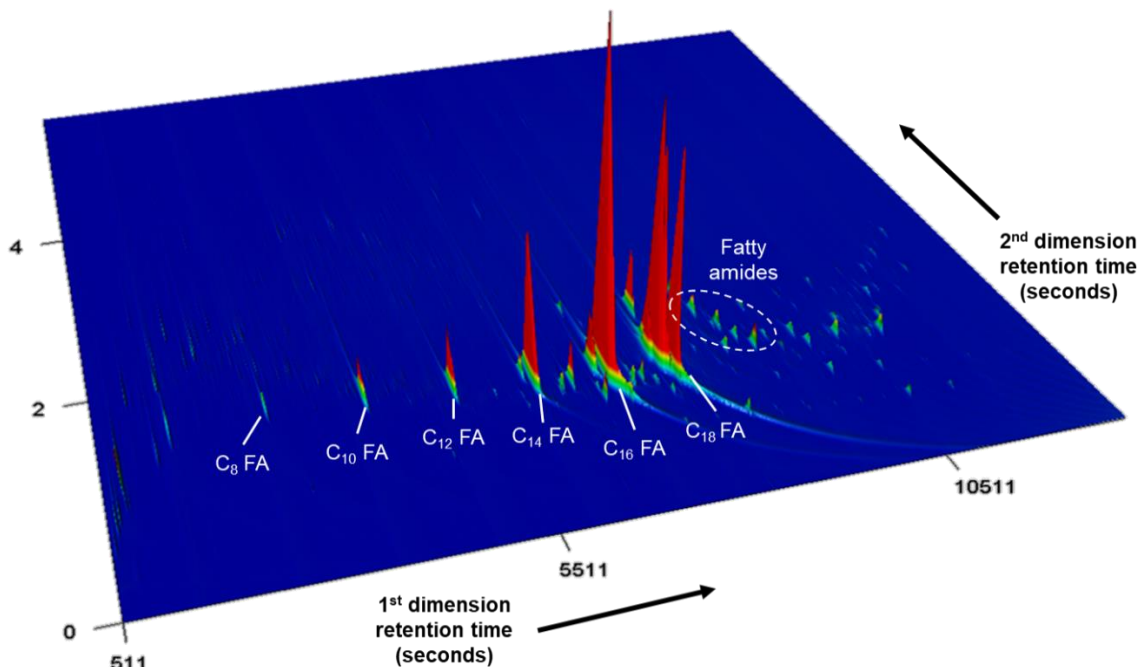


Figure S2. GCxGC-HRT selected ion mountain plot chromatogram from food waste HTL. The primary products identified are C₈ – C₁₈ fatty acids. A group of fatty amides is also present in moderate abundance.

Table S2. Chemical name for all identified reactants and products in the kinetic model studied.

	Chemical Name	Schemes	Species Class
M1	glycine	1, 2, 3, 4, 5, 6	Amino Acid
M2	hydrogen	1	Gas
M3	water	1, 2, 3, 4, 5, 6	Water
M4	ammonia	1	Gas
M5	carbon dioxide	1, 2, 3, 5	Gas
M6	2-iminoacetic acid	1	Imine
M7	buta-1,3-diene	1, 2, 3, 4	Diene
M8	2-hydroacetic acid	1	Hydroxy-acid
M9	acetic acid	1	Carboxylic acid
M10	methanamine	1, 2	Amine
M11	1,2,3,6-tetrahydropyridine-2-carboxylic acid	1	N-heterocycle
M12	formaldehyde	2, 3	Aldehyde
M13	(hydroxymethyl)glycine	2	Hemiaminal
M14	2-(methyleneamino) acetic acid	2	Schiff base
M15	2-(3,6-dihydropyridin-1(2H)-yl) acetic acid	2	N-heterocycle
M16	N- methylmethanimine	2	Schiff base
M17	(methylamino) methanol	2	Alkanolamine
M18	furfural	3	Aldehyde
M19	(furan-2-yl(hydroxy)methyl) glycine	3	Hemiaminal
M20	(Z)-2-((furan-2- ylmethylene)amino)acetic acid	3	Schiff base

M21	2-(2-(furan-2-yl)-3,6-dihydropyridin-1(2H)-yl)acetic acid	3	N-heterocycle
M22	(Z)-1-(furan-2-yl)-Nmethylmethanimine	3	Schiff base
M23	N-(furan-2-ylmethyl)methanimine	3	Schiff base
M24	((furan-2-ylmethyl)amino)methanol	3	Alkanolamine
M25	furan-2-ylmethanamine	3	Amine
M26	(S)-2,3-dihydroxypropanal; glyceraldehyde	4	Aldehyde
M27	((2S)-1,2,3-trihydroxypropyl)glycine	4	Hemiaminal
M28	(R,Z)-2-((2,3-dihydroxypropylidene)amino)acetic acid	4	Schiff base
M29	2-(2-((R)-1,2-dihydroxyethyl)-3,6-dihydropyridin-1(2H)-yl)acetic acid	4	N-heterocycle
M30	(Z)-(2,3-dihydroxyprop-1-en-1-yl)glycine	4	Enamine
M31	(3-hydroxy-2-oxopropyl)glycine	4	Amadori
M32	(Z)-(2,3-dihydroxyallyl)glycine	4	Enediol
M33	2-hydroxyacrylaldehyde	4	Aldehyde
M34	2-oxopropanal; pyruvaldehyde	4	Dicarbonyl
M35	oxalaldehyde; glyoxal	5	Aldehyde
M36	(1-hydroxy-2-oxoethyl)glycine	5	Hemiaminal
M37	(Z)-2-((2-oxoethylidene)amino)acetic acid	5	Schiff base
M38	(Z)-2-(methyleneamino)ethen-1-ol	5	Schiff base
M39	2-(methyleneamino)acetaldehyde	5	Amino-aldehyde
M40	2-((hydroxymethyl)amino)acetaldehyde	5	Amino-aldehyde
M41	2-aminoacetaldehyde	5	Amino-aldehyde
M42	2-((2-amino-1-hydroxyethyl)amino)acetaldehyde	5	Amino-aldehyde
M43	piperazine-2,5-diol	5	N-heterocycle
M44	1,2,3,6-tetrahydropyrazin-2-ol	5	N-heterocycle
M45	2,5-dihydropyrazine	5	N-heterocycle
M46	glycylglycine	6	Amide
M47	piperazine-2,5-dione	6	N-heterocycle

Table S3. Summary of all reactions, rate expression (mol/cm³/s), Gibbs energy of activation at 600 K, and chemical class.

Rxn #	Reaction	r _j	ΔG_{ts} (kcal/mol)	Class*
Scheme 1				
1.1	$M_1 \rightarrow M_2 + M_6$	$k_j[M_1]$	107.24	Degradation
1.2	$M_6 + M_7 \rightarrow M_{11}$	$k_j[M_6][M_7]$	45.80	ADA*
1.3	$M_1 + M_3 \rightarrow M_4 + M_8$	$k_j[M_3][M_1]$	106.93	Deamination*
1.4	$M_1 + M_2 \rightarrow M_4 + M_9$	$k_j[M_1][M_2]$	108.83	Deamination*

1.5	$M_1 \rightarrow M_5 + M_{10}$	$k_j [M_1]$	73.5	Decarboxylation*
Scheme 2				
2.1	$M_1 + M_{12} \rightarrow M_{13}$	$k_j[M_1][M_{12}]$	49.23	Combination
2.2	$M_{13} \rightarrow M_3 + M_{14}$	$k_j [M_{13}]$	57.44	Dehydration
2.3	$M_{14} + M_7 \rightarrow M_{15}$	$k_j[M_{14}][M_7]$	52.32	ADA*
2.4	$M_{14} \rightarrow M_5 + M_{16}$	$k_j [M_{14}]$	70.44	Decarboxylation*
2.5	$M_{16} + M_3 \rightarrow M_{17}$	$k_j [M_{16}][M_3]$	63.70	H2O addition
2.6	$M_{17} \rightarrow M_{12} + M_{10}$	$k_j [M_{17}]$	39.66	Degradation
Scheme 3				
3.1	$M_1 + M_{18} \rightarrow M_{19}$	$k_j[M_1][M_{18}]$	51.90	Combination
3.2	$M_{19} \rightarrow M_{20} + M_3$	$k_j[M_{19}]$	51.04	Dehydration
3.3	$M_{20} + M_7 \rightarrow M_{21}$	$k_j[M_{20}][M_7]$	55.74	ADA*
3.4	$M_{20} \rightarrow M_5 + M_{22}$	$k_j[M_{20}]$	71.24	Decarboxylation*
3.5	$M_{22} \rightarrow M_{23}$	$k_j [M_{22}]$	77.44	Rearrangement
3.6	$M_{23} + M_3 \rightarrow M_{24}$	$k_j[M_{23}][M_3]$	65.73	H2O addition
3.7	$M_{24} \rightarrow M_{12} + M_{25}$	$k_j[M_{24}]$	38.39	remove CH2O
Scheme 4				
4.1	$M_1 + M_{26} \rightarrow M_{27}$	$k_j[M_1][M_{26}]$	48.94	Combination
4.2	$M_{27} \rightarrow M_3 + M_{28}$	$k_j[M_{27}]$	55.71	Dehydration
4.3	$M_{28} + M_7 \rightarrow M_{29}$	$k_j[M_{28}][M_7]$	50.15	ADA*
4.4	$M_{28} \rightarrow M_{30}$	$k_j[M_{28}]$	59.48	Rearrangement
4.5	$M_{30} \rightarrow M_{31}$	$k_j[M_{30}]$	68.95	Rearrangement
4.6	$M_{31} \rightarrow M_{32}$	$k_j[M_{31}]$	64.13	Rearrangement
4.7	$M_{32} \rightarrow M_1 + M_{33}$	$k_j[M_{32}]$	29.60	Degradation
4.8	$M_{33} \rightarrow M_{34}$	$k_j[M_{33}]$	64.30	Rearrangement
Scheme 5				
5.1	$M_1 + M_{35} \rightarrow M_{36}$	$k_j[M_1][M_{35}]$	45.35	Combination
5.2	$M_{36} \rightarrow M_3 + M_{37}$	$k_j[M_{36}]$	61.14	Dehydration
5.3	$M_{37} \rightarrow M_5 + M_{38}$	$k_j[M_{37}]$	37.40	Decarboxylation
5.4	$M_{38} \rightarrow M_{39}$	$k_j[M_{38}]$	55.62	H2O addition
5.5	$M_{39} + M_3 \rightarrow M_{40}$	$k_j[M_{39}][M_3]$	65.57	Decomposition
5.6	$M_{40} \rightarrow M_{41} + M_{12}$	$k_j[M_{40}]$	40.26	Addition
5.7	$2M_{41} \rightarrow M_{42}$	$k_j[M_{41}][M_{41}]$	53.65	Rearrangement
5.8	$M_{42} \rightarrow M_{43}$	$k_j[M_{42}]$	40.79	Dehydration

5.9	$M_{43} \rightarrow M_{44} + M_3$	$k_j[M_{43}]$	50.58	Dehydration
5.10	$M_{44} \rightarrow M_{45} + M_3$	$k_j[M_{44}]$	-0.21	Dehydration
Scheme 6				
6.1	$2M_1 \rightarrow M_{46}$	$k_j[M_1][M_1]$	64.35	Coupling
6.2	$M_{46} \rightarrow M_{47} + M_3$	$k_j[M_{46}]$	71.74	Condensation*

*Indicates primary reaction mechanism corresponding to colors in Figure 4.

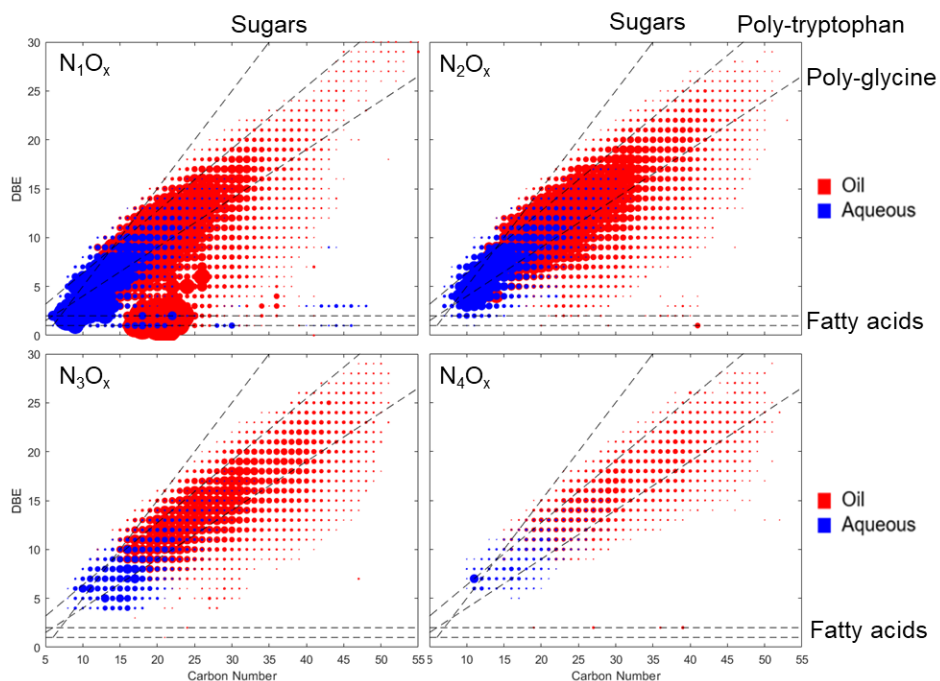


Figure S3. Double bond equivalency (DBE) dependance on carbon number for four primary nitrogen classes seen in food waste HTL products including predictive lines representing sugar, fatty acid, and two poly-amino acids. Datapoints sized by relative abundance.

For the biocrude phase, FT-MS reveals the average empirical formula as $C_{29}H_{36}N_2O_3$ and $C_{12}H_{17}NO_2$ for the aqueous phase, a difference solely in carbon number. This is in comparison to elemental analysis which predicts an oil-phase empirical formula of $C_{21}H_{31}NO_4$. The effect can be further observed by comparing the molecular distributions in each phase. FT-MS predicts a CHONS molecular formula and relative abundance for each molecule detected, which allows a DBE to be calculated. ($DBE = C - \frac{H}{2} + \frac{N}{2} + 1$). Utilizing this formula, **Figure S3** showcases the linearity that exists between carbon number and DBE for both oil and aqueous phases among heteroatom classes. The relationship demonstrates a continuum across the two product fractions showing how lower carbon number molecules, with a lower DBE, tend to partition to the aqueous phase, while molecules of a larger carbon number and DBE are found in the oil phase. Additionally, the presence of the dashed lines bound the product distribution by showing the feed

ratios from saturated and unsaturated fatty acids, as well as sugar dimers. In the N_1O_x class, the intense region centered around C_{20} at $DBE < 5$ is representative of a high abundance of fatty acid amides in the oil phase. It can also be seen that a small amount of these molecules were also found in the aqueous phase, potentially indicating incomplete phase separation due to equilibrium, as these compounds typically have a partition coefficient < 5 . The presence of fatty acid amides arises from the reaction of fatty acids from the hydrolysis of triglycerides with amines from protein degradation.²⁰

The size of the points in **Figure S3** directly correspond to their relative abundance, indicating a higher overall abundance in the N_1O_x and N_2O_x classes compared to the N_3O_x and N_4O_x classes. A shift can also be seen in the location of the high abundance compounds in each class, wherein the N_1O_x class begins near C_5 , $DBE = 1$ and the N_4O_x class does not show molecules until above C_{10} , $DBE = 5$ therefore indicating dimerization to high molecular weight nitrogen heterocycles. The apparent linear trend of the response data falls between that of the sugar molecules and the fatty acids. The presence of nitrogen across classes results in a slope of approximately 0.5, indicating that for every one carbon that is added, the DBE increases by 0.5, resulting from the addition of one hydrogen, no nitrogen, and up to two oxygen.

Table S4. Protein, lipid, and carbohydrate content for various algae strains and food waste sources references in this study.

	Protein	Lipid	Carbohydrate	Source
Berbesia m.	22	10	27	Neveux et al.
Nannochloropsis	46	15	36	Neveux et al.
Tetraselmas*	74	13	13	Neveux et al.
Pavlova*	48	22	29	Neveux et al.
Nannochloropsis*	69	20	10	Neveux et al.
Food Waste*	18	22	59	Cheng et al.
Food Waste	32	38	30	This work

*indicates conditions used in Figure 5

Sensitivity Analysis

Sensitivity calculations were completed in MatLab, using the equations shown below. The change in rate constant (k) was evaluated for a 1% perturbation, which was then fed back into the original kinetic model to solve for the new product distribution and resultant concentrations. Sensitivity was plotted for each individual species and reaction, wherein

$$\Delta k = k_i - k_{i-1}$$

$$\Delta C = C_i - C_{i-1}$$

$$Z_{ij} \cong \frac{\Delta C_i}{\Delta k_j}$$

$$\sigma_{ij} = \frac{k_j}{C_i} Z$$

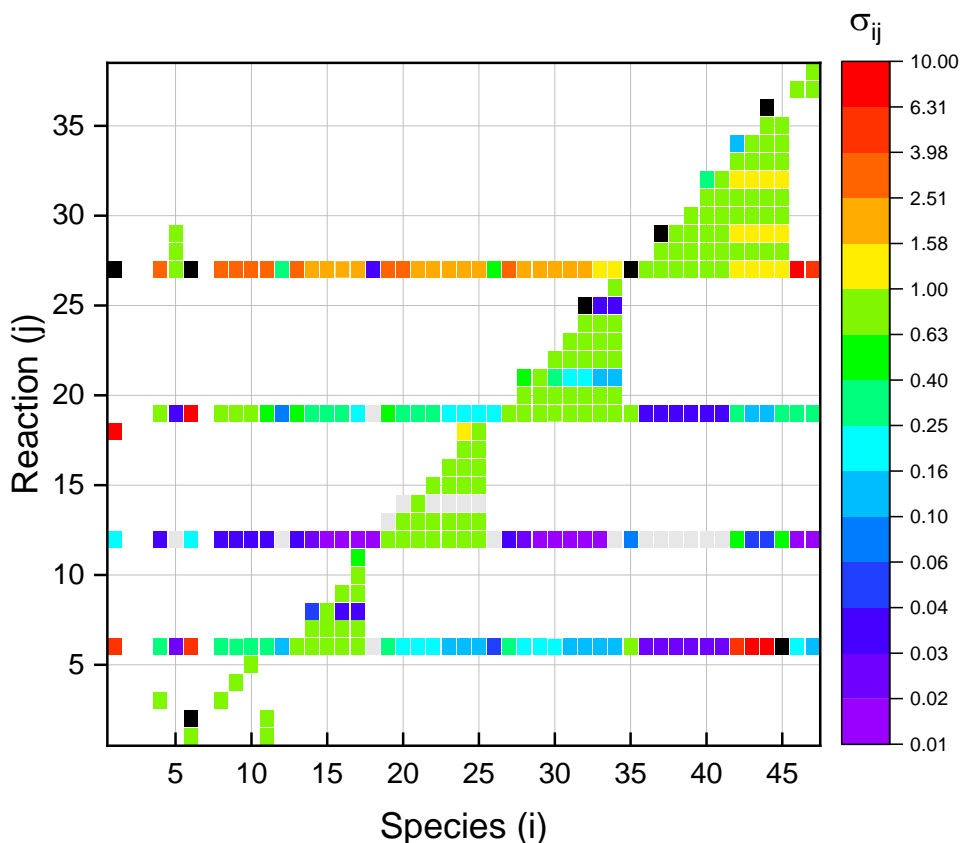


Figure S4. Heatmap showing the average sensitivity of each k value for each species identified in the reaction network. Sensitivity is calculated as an average value across the entire 30 minute reaction window range. Sigma is plotted on a log base 10 scale.

Sensitivity allows for identification of potential model limitations. Analysis of Figure S4 reveals four horizontal lines occurring on reactions 2.1, 3.1, 4.1, and 5.1. This artifact is due to the location of these reactions in the network. Each of these reactions has glycine as a primary reactant, meaning that they are in direct competition with one another. A slight change in the rate of one of these four reactions has the potential to alter the entire product distribution by shifting favorability from one scheme to another. Of these key reactions, scheme 5- the Maillard reaction- appears to result in the highest sensitivity across species. A change in reaction 5.1's reaction rate causes the biggest shift in product distribution, causing an even larger fraction of glycine to proceed through the Maillard reaction.

Supplementary References

1. D. B. Robb and M. W. Blades, *Journal of the American Society for Mass Spectrometry*, 2006, **17**, 130-138.
2. D. B. Robb, T. R. Covey and A. P. Bruins, *Analytical Chemistry*, 2000, **72**, 3653-3659.
3. J. M. Purcell, R. P. Rodgers, C. L. Hendrickson and A. G. Marshall, *Journal of the American Society for Mass Spectrometry*, 2007, **18**, 1265-1273.
4. D. R. Smith, D. B. Robb and M. W. Blades, *Journal of the American Society for Mass Spectrometry*, 2009, **20**, 73-79.
5. J. M. Purcell, C. L. Hendrickson, R. P. Rodgers and A. G. Marshall, *Journal of the American Society for Mass Spectrometry*, 2007, **18**, 1682-1689.
6. J. M. Purcell, C. L. Hendrickson, R. P. Rodgers and A. G. Marshall, *Analytical Chemistry*, 2006, **78**, 5906-5912.
7. N. K. Kaiser, J. P. Quinn, G. T. Blakney, C. L. Hendrickson and A. G. Marshall, *Journal of the American Society for Mass Spectrometry*, 2011, **22**, 1343-1351.
8. G. T. Blakney, C. L. Hendrickson and A. G. Marshall, *International Journal of Mass Spectrometry*, 2011, **306**, 246-252.
9. M. W. Senko, C. L. Hendrickson, M. R. Emmett, S. D. H. Shi and A. G. Marshall, *Journal of the American Society for Mass Spectrometry*, 1997, **8**, 970-976.
10. B. E. Wilcox, C. L. Hendrickson and A. G. Marshall, *Journal of the American Society for Mass Spectrometry*, 2002, **13**, 1304-1312.
11. A. V. Tolmachev, E. W. Robinson, S. Wu, H. Kang, N. M. Lourette, L. Paša-Tolić and R. D. Smith, *Journal of the American Society for Mass Spectrometry*, 2008, **19**, 586-597.
12. N. K. Kaiser, J. J. Savory, A. M. McKenna, J. P. Quinn, C. L. Hendrickson and A. G. Marshall, *Analytical Chemistry*, 2011, **83**, 6907-6910.
13. F. Xian, Y. E. Corilo, C. L. Hendrickson and A. G. Marshall, *International Journal of Mass Spectrometry*, 2012, **325-327**, 67-72.
14. F. Xian, C. L. Hendrickson, G. T. Blakney, S. C. Beu and A. G. Marshall, *Analytical Chemistry*, 2010, **82**, 8807-8812.
15. E. Kendrick, *Analytical Chemistry*, 1963, **35**, 2146-2154.
16. C. A. Hughey, C. L. Hendrickson, R. P. Rodgers, A. G. Marshall and K. Qian, *Analytical Chemistry*, 2001, **73**, 4676-4681.
17. F. W. T. McLafferty, F., *Interpretation of Mass Spectra, 4th ed.*, University Science Books, 4th edn., 1993.
18. J. J. Savory, N. K. Kaiser, A. M. McKenna, F. Xian, G. T. Blakney, R. P. Rodgers, C. L. Hendrickson and A. G. Marshall, *Analytical Chemistry*, 2011, **83**, 1732-1736.
19. Y. E. Corilo, *Journal*, 2014.
20. D. Betancourt-Jimenez, J. P. Youngblood and C. J. Martinez, *ACS Sustainable Chemistry & Engineering*, 2020, **8**, 13683-13691.